George Youssef[1]
Experimental Mechanics Laboratory,
San Diego State University,
5500 Campanile Drive,
San Diego, CA 92182
e-mail: gyoussef@sdsu.edu

Somer Nacy
Experimental Mechanics Laboratory,
San Diego State University,
5500 Campanile Drive,
San Diego, CA 92182;
Department of Biomedical Engineering,
University of Baghdad,
Jaderyia, Baghdad 10071, Iraq
e-mail: nacys2@asme.org

Nha Uyen Huynh
Experimental Mechanics Laboratory,
San Diego State University,
5500 Campanile Drive,
San Diego, CA 92182
e-mail: nhuynh2@sdsu.edu

Mechanics of Microspheres Reinforced Hollow Microcells

Emerging polymeric foams exhibiting unique microstructure of microspherical shells with reinforcing dense microspheres creates a new opportunity for impact-tolerant foam paddings in sport gears applications. This paper describes the static response of reinforced microcell consisting of an outer spherical shell and uniformly distributed microspheres while quantifying the stiffening effect. The distribution of the microspheres is illustrated using the Fourier series, allowing tuning of the reinforcing strategy. Expressions of the external and internal works are derived, whereas the Ritz energy method is adopted to calculate the deformations due to a compressive load distributed over a range of areas. Emphasis is given to the effect of the geometrical attributes of the microcell and the reinforcing microspheres on the resulting deformation response and stiffening effect. The framework is used to investigate the response of several case studies to elucidate the effects of relative radii ratio, reinforcement density, microcell wall thickness, and loading configurations on the stiffness. A new normalized strain energy parameter is introduced to simplify and accelerate the analysis while providing insights on the underpinnings of the observed buckling response. The results strongly suggest the viability of the newly discovered foam microstructure in managing static loads while providing an opportunity to strategically tune the mechanical response using the analytical framework presented herein.
[DOI: 10.1115/1.4049329]

Keywords: energy method, spherical microcells, reinforced microcells, polymeric foams, stiffening effect, mechanical properties of materials, structures

1 Introduction

We consider the problem of the change in the stiffness of microspheres reinforced microcells (spherical shells) under an externally applied load [1–3]. Several new reports have shown that polymeric foams (Fig. 1) with spherical microcellular structure (Figs. 1(*a*) and 1(*b*)) self-formed dense microspheres (Fig. 1(*c*)) during the fabrication process, which were precipitated on the inner surfaces of the spherical microcells. Furthermore, the deposition of the dense microspheres altered the overall mechanical response of the foam. In essence, the microspheres reinforce the walls of the spherical microcells and increase the overall stiffness. The localized experimental probing of the effect of the microspheres on the behavior of each microcell (Fig. 1(*d*)) has proven to be challenging since the isolation of a single cell would disrupt the formation and structure of the unit cell (i.e., microcell and reinforcing microspheres). It is then the objective of this paper to analytically investigate the effect of size, number, distribution, and geometry of the reinforcing microspheres on the overall mechanical response of the unit cell as a function of the applied load. The stiffening effect associated with the addition of reinforcing microspheres is imperative for managing the severity of loading in impact mitigation scenarios. In essence, the problem manifests itself in protective padding used in sports gears by controlling the volumetric changes in the microstructure through the elastic, plateau, and densification regions of polymeric foam behavior.

The broad range of applications is also reflected in the material processing methods, which depend on the unit cell length scale, the material, and the desired performance metrics. The latter can be determined experimentally if individual unit cells can be extracted and tested in controlled conditions congruent to those experienced in deployment. However, analytical and computational modeling approaches have been the prime research methods, given that boundary conditions can be defined to represent deployment conditions accurately. Alternatively, macroscale representative structures can be experimentally tested to validate the underlying performance metric suppositions, e.g., stiffness, impact mitigation, or strength. Taguchi and Kurashige analytically studied the mechanical performance of sintered hollow spheres [4]. They investigated the elastic properties such as Young's modulus, shear modulus, and Poisson's ratio for a model consisting of randomly packed balloons with various degrees of sintering and a wide range of balloon wall thickness. They followed a statistical approach to estimate the macroscopic elastic properties of the packing and proposed a simple formula for these elastic properties. Wei et al. proposed another analytical model for the case of an elastic hollow sphere subjected to diametric point load, where they emphasized the failure mechanism of bulk foams made up of these hollow spheres [5]. Subsequently, Yan and Wei discussed the improved load capacity of hollow spheres foams by optimizing the elastic constants of anisotropic material entrapped in the walls of the spheres [6]. Leveraging a combined theoretical and experimental approach, Shorter et al. studied the axial compression of hollow spheres while reporting a technique to characterize the geometry and the elastic behavior [7].

In addition to the elastic response, buckling and stability analyses of spherical shells under different loads have been extensively studied based on the theorem of work and energy in the inversion of a spherical section [8]. Hutchinson studied the response of complete spherical shells and reported an abrupt mode localization immediately upon the onset of buckling due to the imperfection sensitivity of the structure [9]. Evkin et al. presented an asymptotic solution for thin isotropic spherical shells subjected to a combined load consisting of uniform external pressure and concentrated force at the pole [10]. They validated their results using finite element analysis. Evkin et al. obtained a simple and accurate approximate solution for analyzing the effect of perturbations on the buckling pressure. The stability of thin spherical shells was also investigated using finite element modeling by Niezgodziński and Świniarski [11], reporting the upper limit of the critical loads that causes buckling. Finally, the theoretical and
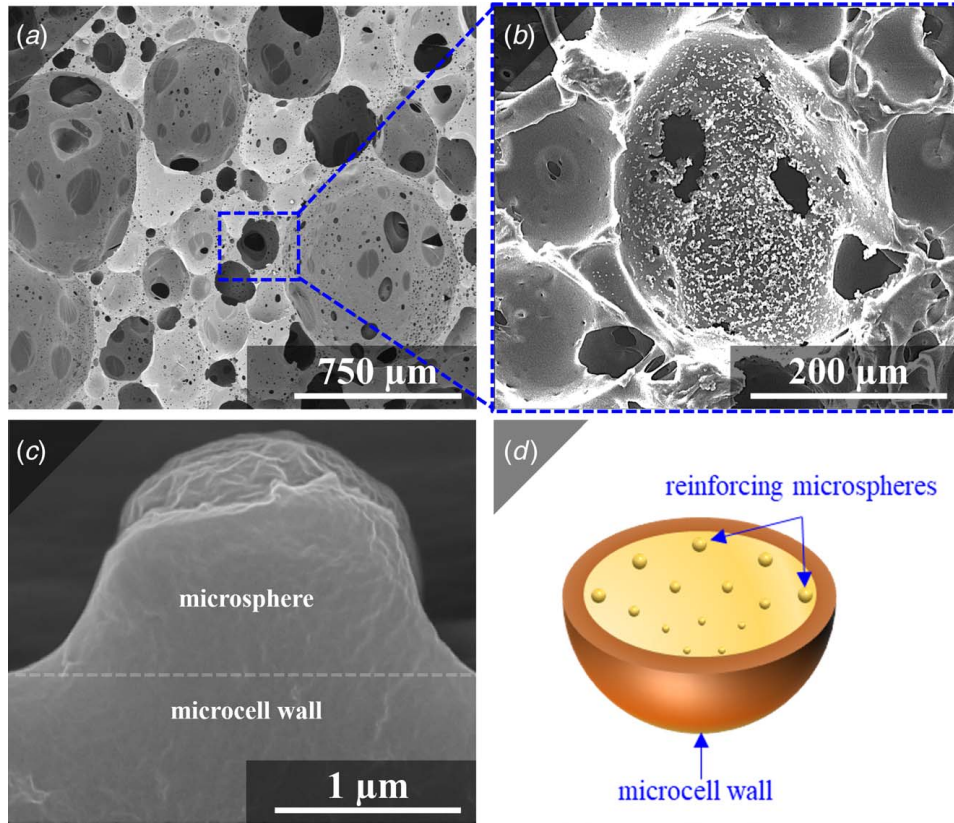
Fig. 1 Extraction of a representative fundamental microcell of polyurea foam (*a*) and (*b*) with the inner wall reinforced with dense microspheres (example shown in (*c*)) made of the same material, and (*d*) schematic representation of the reinforced unit cell

experimental buckling behavior of spherical shells compressed between two rigid plates was reported by Yu et al. [12], which were shown to be in good agreement.

Common to all the studies mentioned above is the investigation of a barren (smooth) spherical shells without additional reinforcement. The objective of the research leading to this paper is to analytically elucidate the difference in the mechanical response of barren (unreinforced) and microsphere reinforced microcellular shells.

2 Description of Kinematics

This section presents the discrete, fundamental unit cell extracted from the micrographs shown in Fig. 1(*d*). The geometrical description (Fig. 2) captures the microcell with reinforcing microspheres distributed in the polar and azimuth directions (e.g., Fig. 2(*b*)), facilitating the derivation of the continuum response. Here, the microcell wall and the dense, reinforcing microspheres are assumed to be of the same material based on previous experimental reports [1].

The microcell (Fig. 2(*a*)) is assumed to be a spherical shell with a uniform wall thickness (*t*) and a diameter of $2r_c$, which can be locally modified by the addition of dense microspheres. The latter is presented as bumps on the inner surface of the microcell and presumed to be ordered in both the azimuth and polar directions with a uniform diameter of $2r_b$. In the polar (ϕ) and azimuth (θ) directions (Fig. 2), the center-to-center distances between two successive bumps are T_ϕ and T_θ, while the ranges are B_ϕ and B_θ, respectively.
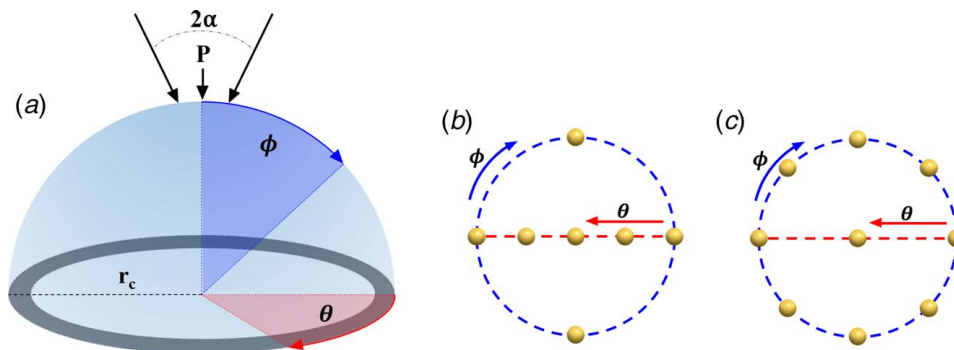

Fig. 2   (*a*) The microcell with the definition of the principal directions and the load configuration, a representative reinforcing case of (*b*) 4 × 8, and (*c*) 8 × 4, showing the difference in the number of microspheres based on the order of the permutation

The distance between the bumps is the periodicity of the reinforcement in the polar and azimuth directions used to independently define their distributions (two examples are shown in Figs. 2(b) and 2(c)).

The two-dimensional distribution of the bumps on the inner surface of the microcell in the polar and azimuth directions can be defined using the Fourier series such that

$$
\begin{aligned}
f(\phi, \theta) =& \sum_{i=0}^{n_\theta} \sum_{j=0}^{n_\phi} a_{ij} \, \cos\left(\frac{2\pi i r_c}{T_\phi}\phi\right) \cos\left(\frac{2\pi j r_c}{T_\theta}\theta\right) \\
&+ \sum_{i=0}^{n_\theta} \sum_{j=0}^{n_\phi} b_{ij} \, \cos\left(\frac{2\pi i r_c}{T_\phi}\phi\right) \sin\left(\frac{2\pi j r_c}{T_\theta}\theta\right) \\
&+ \sum_{i=0}^{n_\theta} \sum_{j=0}^{n_\phi} c_{ij} \, \sin\left(\frac{2\pi i r_c}{T_\phi}\phi\right) \cos\left(\frac{2\pi j r_c}{T_\theta}\theta\right) \\
&+ \sum_{i=0}^{n_\theta} \sum_{j=0}^{n_\phi} d_{ij} \, \sin\left(\frac{2\pi i r_c}{T_\phi}\phi\right) \sin\left(\frac{2\pi j r_c}{T_\theta}\theta\right)
\end{aligned}
\tag{1a}
$$

where n_θ and n_ϕ are the number of reinforcing microspheres in the azimuth and polar directions, respectively. The significance of $f(\phi, \theta)$ lies in its utility to control the distance in the range of the reinforcing microspheres independently, which allows for a broader set of parametric investigations, as discussed in Sec. 3. Therefore, the total number of reinforcing microspheres is $n_\theta((n_\phi/2) - 1) + 2$. The Fourier coefficients (a_{ij}, b_{ij}, c_{ij}, and d_{ij}) are defined as

$$
a_{ij} = \frac{k}{T_\phi T_\theta} \int_0^{T_\theta} \int_0^{T_\phi} g(\phi, \theta) \cos\left(\frac{2\pi i r_c}{T_\phi}\phi\right) \cos\left(\frac{2\pi j r_c}{T_\theta}\theta\right) r_c^2 \, d\phi d\theta
\tag{1b}
$$

$$
b_{ij} = \frac{k}{T_\phi T_\theta} \int_0^{T_\theta} \int_0^{T_\phi} g(\phi, \theta) \cos\left(\frac{2\pi i r_c}{T_\phi}\phi\right) \sin\left(\frac{2\pi j r_c}{T_\theta}\theta\right) r_c^2 \, d\phi d\theta
\tag{1c}
$$

$$
c_{ij} = \frac{k}{T_\phi T_\theta} \int_0^{T_\theta} \int_0^{T_\phi} g(\phi, \theta) \sin\left(\frac{2\pi i r_c}{T_\phi}\phi\right) \cos\left(\frac{2\pi j r_c}{T_\theta}\theta\right) r_c^2 \, d\phi d\theta
\tag{1d}
$$

$$
d_{ij} = \frac{k}{T_\phi T_\theta} \int_0^{T_\theta} \int_0^{T_\phi} g(\phi, \theta) \sin\left(\frac{2\pi i r_c}{T_\phi}\phi\right) \sin\left(\frac{2\pi j r_c}{T_\theta}\theta\right) r_c^2 \, d\phi d\theta
\tag{1e}
$$

In the definition of the Fourier coefficients (Eqs. (1b)–(1e)), k is a constant that is taken to equal 4 when $i, j \neq 0$, 2, when either $i = 0$ or $j = 0$, and 1 for $i, j = 0$. It follows that the periods T_ϕ and T_θ are

$$
T_\phi = \frac{2\pi}{i}(r_c \sin\theta)
\tag{2a}
$$

$$
T_\theta = \frac{2\pi}{j}(r_c \sin\phi)
\tag{2b}
$$

Furthermore, $g(\phi, \theta)$ is a function used to define the location of each reinforcing microsphere based on the distance and period without interference of any two successive microspheres, which is defined as a piecewise continuous function (Fig. 3) that is defined in the polar direction as

$$
g(\phi, \theta) = \begin{cases} 0 & \text{for } 0 \leq r_c\phi < B_\phi \\ 2r_b r_c \phi - (r_c\phi)^2 & \text{for } B_\phi \leq r_c\phi \leq T_\phi \end{cases}
\tag{3a}
$$

and in the azimuth direction as

$$
g(\phi, \theta) = \begin{cases} 0 & \text{for } 0 \leq r_c\theta < B_\theta \\ 2r_b r_c \theta - (r_c\theta)^2 & \text{for } B_\theta \leq r_c\theta \leq T_\theta \end{cases}
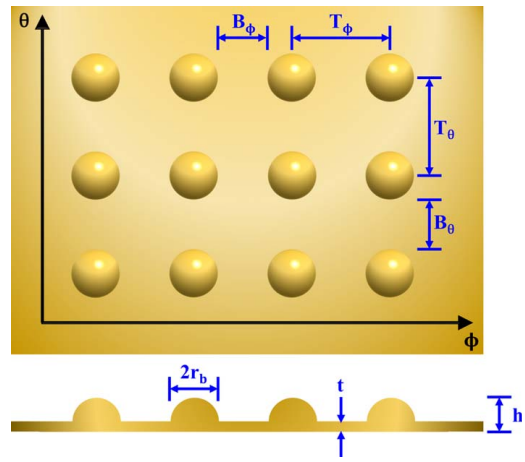\tag{3b}
$$

Fig. 3 Geometrical definitions of the microcell and the reinforcing microspheres attributes, showing the variables used to define the distribution of the bumps

The thickness distribution (Fig. 3) due to the introduction of the reinforcing bumps can then be expressed as

$$
h = t + f(\phi, \theta)
\tag{4}
$$

where t is the wall thickness of the barren microcell.

3 Energy Balance

Figure 2(a) shows the loading configuration considered herein (i.e., the boundary condition), where a load (P) is applied to the external surface of the microcell (see Fig. 2). The load is assumed to be uniformly distributed over the application area, which is defined by the inclination angle (2α) that is symmetrically assigned in the polar and azimuth directions. Therefore, the external work ($\mathfrak{T}$) due to the applied load (P) is

$$
\mathfrak{T} = r_c^3 \int_0^{2\pi} \int_0^\alpha \frac{2P\cos\phi}{h}\left(-\frac{wh}{2r_c} + w\epsilon_\phi + w\epsilon_\theta\right)\sin\phi \, d\phi d\theta
\tag{5}
$$

where the strains (ϵ_ϕ and ϵ_θ) are defined by

$$
\epsilon_\phi = \frac{1}{r_c}\left(\frac{dv}{d\phi} - w\right)
\tag{6a}
$$

$$
\epsilon_\theta = \frac{1}{r_c}(v\cot\phi - w)
\tag{6b}
$$

as a function of the radial (w) and circumferential (v) deformations, respectively. Similarly, the internal work ($\mathfrak{B}$) can be calculated from Eq. (7):

$$
\mathfrak{B} = \frac{r_c^2 E}{1 - \nu^2} \int_0^{2\pi} \int_0^{\pi/2} h(\epsilon_\phi^2 + \epsilon_\theta^2 + 2\nu\epsilon_\phi\epsilon_\theta)\sin\phi \, d\phi d\theta
\tag{7}
$$

where E is the elastic modulus (taken to be 10 MPa) and ν is Poisson's ratio (presumed to be 0.25). It follows that the total potential energy ($\mathfrak{U}$) can be calculated by

$$
\mathfrak{U} = \mathfrak{T} + \mathfrak{B}
\tag{8}
$$

The deformations (v and w) can be found by using the Ritz function and the applied boundary condition

$$
w = a_1 \cos^2\phi + a_2 \cos^2 2\phi
\tag{9a}
$$

$$
v = b_1 \sin^2\phi + b_2 \sin^2 2\phi
\tag{9b}
$$

where, for example, at the pole of the microcell when $\phi = 0$, this condition yields $w = w_{max}$ and $v = 0$. The four unknowns a_1, a_2, b_1, and b_2 in Eqs. (9a) and (9b) can be determined by solving the following equations simultaneously:

$$\frac{\partial \mathfrak{U}}{\partial a_1} = 0, \quad \frac{\partial \mathfrak{U}}{\partial a_2} = 0, \quad \frac{\partial \mathfrak{U}}{\partial b_1} = 0, \quad \text{and} \quad \frac{\partial \mathfrak{U}}{\partial b_2} = 0 \qquad (10)$$

An additional energetic parameter (η) (i.e., normalized strain energy per unit surface area) was used in subsequent analyses to elucidate the underpinning of the observed deformational behavior based on the assumption of constant potential energy while reducing the computational cost. This energetic parameter was defined as a non-dimensional variable to assess the effectiveness of the reinforcement strategy. We opted for this approach over other alternative approaches of resolving integral equations of internal and external work for spatially discretized geometry (i.e., finite element method), which is the emphasis of future work since the focus here was on analytical rather than numerical methods. Another analytical approach, that results in a substantial increase in computational time, is repeating the solution at each combination of ϕ and θ, which is prohibitively expensive to arrive at the cumulative energy over the surface; hence, the energetic cost parameter was defined as

$$\eta = \frac{\mathfrak{B}}{E r_c^3 \int_0^{2\pi} \int_0^{\pi/2} \sin\phi \; d\phi d\theta} \qquad (11)$$

4 Results and Discussion

The model presented above provides an unprecedented utility to investigate the multifaceted effect of reinforcing microspheres, methodically and systematically, to barren microcells. In what follows, the model parameters are individually examined by plotting the resulting deformations with respect to the relative radii of the surface bumps (reinforcing microspheres) and the microcell, the distribution of the microspheres, and the load configuration. At the outset, the overall stiffness of the microcells is elucidated.

4.1 Effect of Relative Radii. Figure 4 shows the normalized deformations of unreinforced, barren microcell ($r_b/r_c = 0$) and a uniformly reinforced microcell with bumps equally distributed in the azimuth and polar directions. The spherical shell wall thickness was taken to be 1 μm throughout the analysis for both barren and

reinforced microcells. The results in Fig. 4 emphasize the effect of relative radii on the microcell mechanical response when the reinforcement effect is taken into account, where three relative radii ratios are considered: $r_b/r_c = 0.10$, $r_b/r_c = 0.15$, and $r_b/r_c = 0.20$. Regardless of the reinforcement configuration, the response is plotted based on a 30 N load applied symmetrically over $2\alpha = 6$ deg. The microcell radius is kept constant at 70 μm, which is experimentally based on the average diameter of polyurea foam with a similar microstructure reported a priori [1–3]. As expected, the barren microcell experiences the most considerable deformation and even showing the onset of buckling. The maximum deformation is reported for the barren microcell, where the pole is compressed by 29.4% while the equator expanded by 25%. The difference in the polar and azimuth deformations at the pole and equator is attributed to the microcell wall buckling at a location closer to the pole than the equator, which is also affected by other exchanges between the internal and external works, as discussed next based on η from Eq. (11). The mechanical response of the barren microcell reported in Fig. 4, including the elastic instability, is consistent with the results from the investigation of a spherical shell made by Shorter et al. [7], where the behavior of the responses are found to be in good agreement. On the other hand, the reinforced microcells reported 19%, 5.2%, and 2.1% lower deformations, at the pole, than the unreinforced microcell for $r_b/r_c = 0.10$, $r_b/r_c = 0.15$, and $r_b/r_c = 0.20$, respectively. That is to say, enlarging the diameter of the reinforcing microspheres (surface bumps) increases the overall resistance to deformation. Interestingly, the deformed shape for $r_b/r_c = 0.20$ is merely 2%, on average, away from the undeformed circumference, with 12 micro-bumps in each direction (62 bumps on the inner wall surface) and covering 62% of the surface area, resulting in a 13-fold increase in stiffness. Contrary to the barren microcell, none of the cases of reinforced microcells exhibit buckling despite being subjected to the same loading conditions. Therefore, the results in Fig. 4 unequivocally support the hypothesis that the addition of microspheres reinforces the investigated microcells by increasing the stiffness and delaying the onset of elastic instability under the same loading conditions. The mechanical properties of polymeric foams with reinforced microcells were shown experimentally to be superior to their counterparts with barren unit cells [2,3].

As mentioned above, the deformations at the pole and equator, regardless of the reinforcement condition, exhibit a notable difference, where the former is persistently higher than the latter. This is better elucidated by examining the values of the newly introduced energetic cost parameter (η), based on the change in the strain
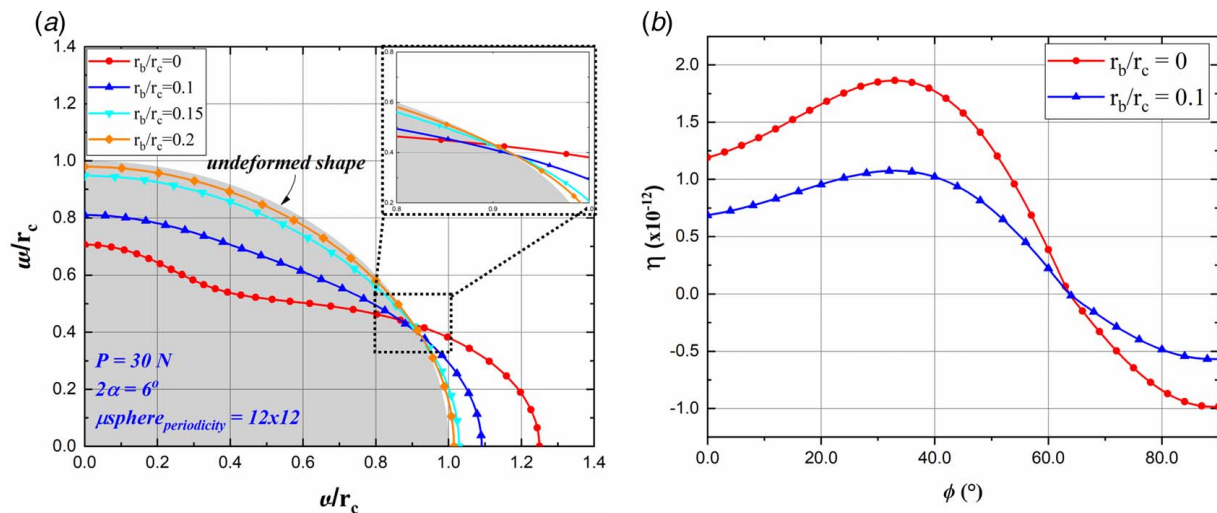
Fig. 4 (a) Normalized deformation of a barren ($r_b/r_c = 0$) and reinforced microcell based on an applied load of 30 N at constant microsphere periodicity of the reinforcing bumps, and (b) normalized strain energy parameter as a function of the polar angle ϕ. The barren microcells exhibit significant deformations compared with their reinforced counterparts

energy. Figure 4(b) shows the resulting values of η for the case of barren and reinforced microcells under similar loading conditions, as discussed above. For the latter, we only consider the configuration of 62 uniformly distributed surface micro-bumps, without the loss of generality. The η values for the barren microcell case are consistently higher than their reinforced counterparts, indicating the increased deformation (Fig. 4(a)) or reduced resistance to deformation. The location of maximum η coincides with the location of buckling instability, which is also the location of maximum deformation. Finally, the microcell sheath appears to be fixed or having zero deformation at the steepest slope (for ϕ ranging from ~40 deg to ~60 deg) leading to the node location, or inflection point. Hence, investigating the behavior of the energetic cost parameter leads to (1) identifying the location of the maximum deformation (at which elastic instability would be expected), (2) pinpointing the position of the node, and (3) explicating the difference between the pole and equator deformations. It is also worth noting the dependence of the deformation on the radius of the reinforcing microspheres, where the internal work is directly proportional to r_b, as shown in Eq. (7). That is to say, as shown in Fig. 4(a) and as discussed above, enlargement in the diameter of the reinforcing surface bumps stiffens the response and reduces the deformation.

4.2 Effect of Reinforcement Density.

In Sec. 4.1, the mere existence of reinforcing microspheres on the microcell surface results in the reduction of the reported deformations for the same loading scenario, leading to the conclusion of an increase in the stiffness. Nonetheless, the model formulation provides the utility to independently investigate the influence of the reinforcing microsphere distribution on the overall deformation by controlling the number of surface bumps in the azimuth and polar directions separately. Figure 5 shows the results of changing the density of the reinforcing microspheres on the deformation of the microspherical shell compared with the deformation of a barren microcell. The number of microspheres in each direction ranges from 4 to 28, with an increment of four bumps. For each set of azimuth and polar reinforcement conditions, the results are obtained for a given permutation, e.g., 4×12 and 12×4. The applied load is kept constant at 50 N distributed symmetrically over $2\alpha = 6$ deg. The remaining geometrical parameters are set to: $r_b/r_c = 0.10$ and $t/r_c = 0.02$ with $r_c = 70 \ \mu m$. The mechanical response shown in Fig. 5 is summarized into three overarching observations. First, the change in the permutation of each subset results in a slightly different deformation. For example, the normalized polar deformation for 28×12 is 0.80, while it is 0.79 for 12×28. Logically, the deformation percentage changes as a function of the number of reinforcing microspheres,

as discussed earlier, but the difference due to rearranging the permutation persists. This leads to the second observation, where the increase in the surface coverage, by increasing the population of micro-bumps, affects the deformation response. As the total number of the reinforcing microspheres increases from 14 to 254, the normalized deformation at the pole and equator decreases from 0.42 and 0.35 to 0.15 and 0.13, respectively. At the lower population limit investigated here, the microspheres cover 3.5% of the surface area, increasing to 65.5% at the upper limit signifying the ample opportunity to enhance the reinforcement effect further. Finally, the maximum buckling deformation decreases (see inset in Fig. 5) as a function of the increasing microsphere population, where a normalized maximum deformation is found to be 0.47 for the barren microcell, and 0.15 for the case of 262 reinforcing microspheres. This final observation is consistent with the results discussed in Sec. 4.1 regarding the reinforcing effect. In all, these three observations are symbiotically related to the total number of reinforcing microspheres as well as the location of the latter with respect to the applied load, discussed next.

4.3 Effect of Microcell Wall Thickness.

The deformation of the barren or reinforced microcell is also dependent on the microcell wall thickness, given its contribution to the overall thickness, as shown in Eq. (4). Figure 6 shows the results of the normalized deformations for different microcell thickness to radius ratios (t/r_c) ranging from 0.02 to 0.10, while maintaining the applied load at 250 N over $2\alpha = 4$ deg and holding $r_b/r_c = 0.10$. As expected, an increase in the microcell thickness to radius ratio leads to a substantial reduction in the normalized deformation. Two noteworthy observations are warranted here. First, the wall thickness reduction results in instigating elastic instability, even when the microcell is reinforced with 62 microspheres. This is contrary to what has been discussed above, where the reinforcement consistently stiffens the response and eliminates the conditions leading to buckling. In other words, an effective reinforcement configuration is only guaranteed after the proper selection of t/r_c ratio. Second, the node location signifying the inflection point of the deformation shifts from inside or on the undeformed shape (as it was the case for all the examples discussed in Secs. 4.1 and 4.2) to the outside. While the shift appears to be minimal, it notably indicates the possibility of leveraging the t/r_c in the development of the microstructure of polymeric foams that is more tolerant to the energy from incoming impacts. From an experimental point of view, the t/r_c can be adjusted by controlling the foaming (or blowing) agent, which continues to expand the diameter of the microcell while thinning the wall thickness, as discussed in Ref. [1].
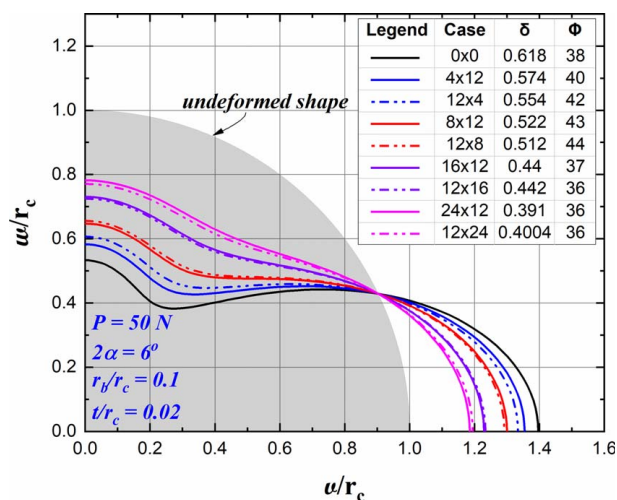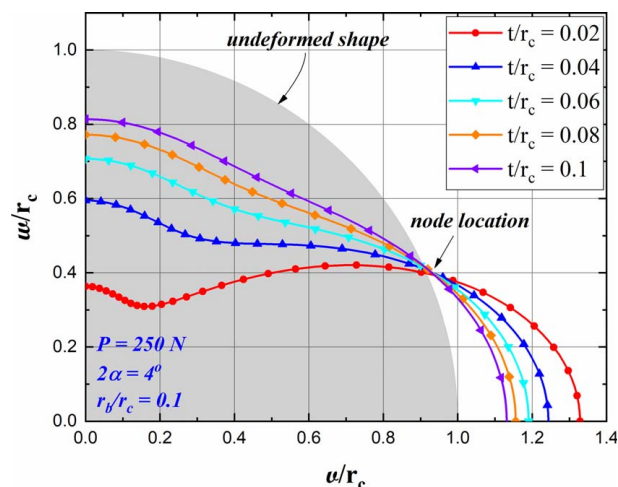

Fig. 5 Effect of the distribution of the reinforcing microspheres on the normalized deformations, showing the slight difference based on the order of the permutations

Legend	Case	δ	Φ
	0x0	0.618	38
	4x12	0.574	40
	12x4	0.554	42
	8x12	0.522	43
	12x8	0.512	44
	16x12	0.44	37
	12x16	0.442	36
	24x12	0.391	36
	12x24	0.4004	36

Fig. 6 Effect of the variation microcell thickness on the normalized deformations for the same reinforced case
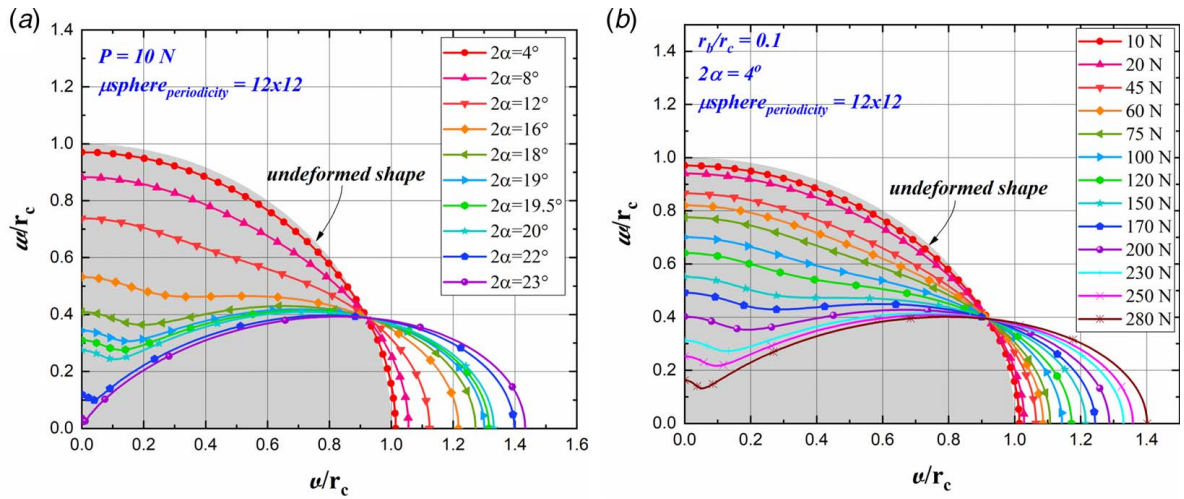
Fig. 7 Effect of loading configuration on the resulting normalized deformation with the influence of (*a*) the loading area and (*b*) load magnitude

4.4 Effect of Loading Configuration. Here, the loading configuration is defined as the interplay between the magnitude of the applied load (P) and the area over which it is distributed (2α). Figure 7(*a*) shows the normalized deformation of reinforced microcell with 62 microspheres distributed uniformly in the azimuth and polar directions with the load application region ranging from 4 deg to 23 deg, representing 18.75 μm^2 to 612 μm^2 surface area and a 10 N constant load. The normalized deformations increase as the loading region increases, reaching nearly a total collapse under the loading tip for $2\alpha = 23$ deg. It is worth noting that buckling instability is initially observed when $2\alpha = 16$ deg, where the strain energy is sufficient for this condition to occur. Further increase in the load application region results in a more pronounced buckling deformation until the collapse took place, as expected. Over the range of investigated load application regions, only two buckling modes are observed, those starting at $2\alpha = 16$ deg and $2\alpha = 23$ deg, which is mechanistically consistent with the results of the considered boundary conditions and shown experimentally by Shorter et al. [7]. Such elastic deformation is highly desirable in polymeric foams because (1) it signifies recoverable deformation where the foam padding can sustain repeated loading (recently demonstrated experimentally by our group [13]), and (2) it implies large energy dissipation due to buckling to shunt the energy protecting human brains from a concussion in biomechanical impact scenarios [14].

On the other hand, the normalized deformation results in Fig. 7(*b*) demonstrate the effect of increasing load magnitude for the same reinforced microcell. In this case, the load application region is kept constant at $2\alpha = 4$ deg, the relative radii ratio is taken as $r_b/r_c = 0.10$, and uniformly distributed 62 reinforcing microspheres, while the applied load ranges from 10 N to 280 N. Remarkably, such a high load of 280 N applied over a relatively small region on a microcell with a diameter of 140 μm does not result in total collapse, as it is the case of $2\alpha = 23$ deg with merely 3.6% of the load. This loading capacity can be further tuned by either changing the geometrical attributes of the microcell and microspheres or by strategically increasing the population of the surface bumps, as discussed earlier. Nonetheless, an increasing applied load yields higher normalized overall and buckling deformations, where the onset of the latter is first observed at 100 N.

4.5 Microcell Stiffness. The stiffness of any structure is a function of geometry and material properties. In the case under consideration, the microcell stiffness depends on its thickness and radius, and the number, size, and distribution or periodicity of the reinforcing microspheres. The material properties generally play a significant role but are assumed as unvaried in this investigation. Therefore, two normalized factors are defined to elucidate the interdependence of stiffness and geometrical attributes, the microsphere to microcell radii ratio (r_b/r_c), and the number of microspheres in the ϕ and θ directions (represented as $n_\phi \times n_\theta$). Figure 8(*a*) shows the stiffness as a function of the number of reinforcing microspheres, where the lower bound is based on the case of a barren microcell with a uniform thickness (taken to be 1 μm) and the upper bound is defined based on the response of an unreinforced microcell with a uniform thickness of $t + r_b$. Generally, and as discussed earlier, increasing the population of reinforcing microspheres influences the resulting overall stiffness positively, where the latter is also dependent on the distribution of the surface bumps along the azimuth and polar directions. The stiffness change with respect to the number of microspheres is found to be ~125.2 kN/m/n_θ and ~117.6 kN/m/n_ϕ while separately keeping n_ϕ and n_θ constant at 20, respectively. This indicates that reinforcing by adjusting n_ϕ is more effective than increasing the overall stiffness of the microcell. In other words, increasing n_ϕ while maintaining n_θ constant is the most beneficial strategy for stiffening the microcell.

Figure 8(*a*) also shows that increasing the reinforcing microspheres and radii ratio significantly affects the surface coverage area. For example, the stiffness is 3.4 MN/m when $r_b/r_c = 0.10$ and $n_\phi \times n_\theta = 16 \times 20$, while it is 7.8 MN/m for $r_b/r_c = 0.15$ and the same number of microspheres. In other words, increasing the radii ratio by 50% results in a 2.3-fold increase in the stiffness, which is attributed to a corresponding change in the surface coverage area. Increasing the radii ratio indicates the enlargement of the reinforcing microspheres diameter, which, in turn, occupy a larger footprint on the inner surface of the microcell. The same number of reinforcing microspheres (16×20) covers 35.5% and ~80% of the inner surface area of the microcell for the case of $r_b/r_c = 0.10$ and $r_b/r_c = 0.15$, respectively. This more than a twofold increase in the coverage area reduces the strain energy due to the stiffening of the deformation response, which is succinctly summarized in the plot of the energetic cost parameter (η) shown in Fig. 8(*b*). Here, we reach the trivial solution for the stiffness enhancement mechanism by increasing the microcell wall thickness. The results in Fig. 8(*b*) also signify the importance of controlling the relative radii ratio, regardless of the reinforcing configuration, since it translates to a significant energy change. It is important to note that the negligible effect of the reinforcing configuration, discussed previously, is further demonstrated by comparing the values of η for different numbers of surface micro-bumps based on alternate permutation such as the case for 16×12 or 12×16, for example.
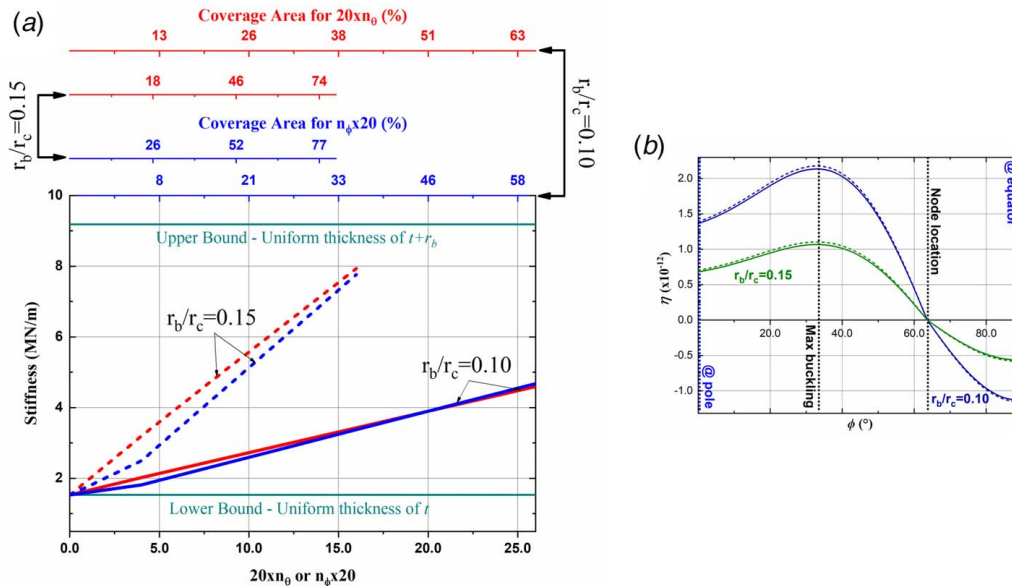
Fig. 8 (*a*) Overall stiffness of the reinforced microcell defining the lower and upper bounds, and (*b*) the normalized strain energy as a function of the polar angle ϕ for different permutation of the reinforcing microspheres

4.6 Model Limitations. The modeling framework discussed above sheds new light on the mechanics of barren and reinforced microcells as a function of different geometrical and loading attributes. However, there are several limitations to the existing framework, constituting the future directions of this research. Future research can expand the model applicability to include material nonlinearities such as the hyperelastic response of polymers or geometrical nonlinearities by accounting for the surface proliferations shown in Fig. 1(*a*) and also reported in Ref. [15]. The model can be further developed to study the interactions between neighboring microcells in a representative volume element consisting of several microcells in various spatial configurations. Several necessary loading conditions will also be at the center of future investigations, including uniform pressure applied, internally or externally, to the entire or portions of the barren or reinforced microcells. The current model assumes the load to be static, contrary to what is expected in impact mitigation application. Therefore, the time-dependent properties of the materials (e.g., viscoelastic properties) and time-varying forces or pressures will be applied while parametrically monitoring the mechanical response as a function of time in the future. Therefore, these future directions also summarize the main limitations of the current model.

5 Conclusion

The analysis conducted throughout this work consists of observing the static response, i.e., deformation, for a thin elastic hollow microcell with internal uniformly distributed microspheres, under the effect of an external load. The procedure is achieved through analytical modeling the microcell inner surface topography and applying the Ritz energy method to solve for the deformations. A newly introduced normalized strain energy parameter is found to simplify the analysis by reducing the computational cost and explicating the observed buckling response. The buckled region coincides with the maximum normalized strain energy location, and the node of zero deformation corresponds to zero normalized strain energy. The stiffness of the reinforced microcell hinges on the convulsed effects of microcell thickness, size, and distribution of the reinforcing microspheres, and the external loading. The analytical results are found to be supported by recent experimental investigations of the response of polymeric foams. This research

is considered as the impetus of future analyses, in which the static and dynamic responses of different hollow geometries can be investigated under various loading and boundary conditions. The future directions, based on the limitations of the current modeling framework, are clearly discussed.

Conflict of Interest

There are no conflicts of interest.

Data Availability Statement

The raw/processed data required to reproduce these findings cannot be shared at this time as the data also form part of an ongoing study.

References

[1] Do, S., Huynh, N. U., Reed, N., Shaik, A. M., Nacy, S., and Youssef, G., 2020, "Partially-Perforated Self-Reinforced Polyurea Foams," Appl. Sci., **10**(17).
[2] Reed, N., Huynh, N. U., Rosenow, B., Manlulu, K., and Youssef, G., 2019, "Synthesis and Characterization of Elastomeric Polyurea Foam," J. Appl. Polym. Sci., **137**(26), pp. 1–8.
[3] Youssef, G., Reed, N., Huynh, N. U., Rosenow, B., and Manlulu, K., 2021, "Experimentally-Validated Predictions of Impact Response of Polyurea Foams Using Viscoelasticity Based on Bulk Properties," J. Eng. Mater. Technol., **143**(1), p. 011001.
[4] Taguchi, I., and Kurashige, M., 2007, "Macroscopic Elastic Properties of Randomly Packed Balloons," J. Mech. Mater. Struct., **2**(3), pp. 529–556.
[5] Wei, X. X., Wang, Z. M., and Xiong, J., 2015, "The Analytical Solutions for the Stress Distributions Within Elastic Hollow Spheres Under the Diametrical Point Loads," Arch. Appl. Mech., **85**(6), pp. 817–830.

[6] Yan, L., and Wei, X., 2019, "An Analytical Solution for the Stress Distribution Within a Spherically Isotropic Hollow Sphere Under Diametrical Compression," Math. Mech. Solids, **24**(5), pp. 1256–1278.

[7] Shorter, R., Smith, J. D., Coveney, V. A., and Busfield, J. J. C., 2010, "Axial Compression of Hollow Elastic Spheres," J. Mech. Mater. Struct., **5**(5), pp. 693–705.

[8] Khakina, P. N., 2013, "Buckling Load of Thin Spherical Shells Based on the Theorem of Work and Energy," Int. J. Eng. Technol., **5**(3), pp. 392–394.

[9] Hutchinson, J. W., 2016, "Buckling of Spherical Shells Revisited," Proc. R. Soc. A Math. Phys. Eng. Sci., **472**(2195).

[10] Evkin, A., Kolesnikov, M., and Prikazchikov, D. A., 2017, "Buckling of a Spherical Shell Under External Pressure and Inward Concentrated Load: Asymptotic Solution," Math. Mech. Solids, **22**(6), pp. 1425–1437.

[11] Niezgodziński, T., and Świniarski, J., 2010, "Numerical Calculations of Stability of Spherical Shells," Mech. Mech. Eng., **14**(2), pp. 325–337.

[12] Yu, W., Li, H., Liang, X., He, C., and Wang, M., 2011, "Experimental and Theoretical Studies on Buckling of Thin-Walled MHS Compressed Between Two Rigid Plates," Arch. Appl. Mech., **81**(12), pp. 1827–1832.

[13] Koohbor, B., Blourchian, A., Uddin, K. Z., and Youssef, G., 2020, "Characterization of Energy Absorption and Strain Rate Sensitivity of a Novel Elastomeric Polyurea Foam," Adv. Eng. Mater., **2000797**, pp. 1–11.

[14] Uddin, K. Z., Youssef, G., Trkov, M., Seyyedhosseinzadeh, H., and Koohbor, B., 2020, "Gradient Optimization of Multi-Layered Density-Graded Foam Laminates for Footwear Material Design," J. Biomech., **109**, p. 109950.

[15] Ramirez, B. J., and Gupta, V., 2019, "Energy Absorption and Low Velocity Impact Response of Open-Cell Polyurea Foams," J. Dyn. Behav. Mater., **5**(2), pp. 132–142.